MNRAS 000, 1–?? (2016) Preprint January 25, 2017 Compiled using MNRAS LATEX style file v3.0

Synthetic absorption lines for a clumpy medium: a spectral signature for cloud acceleration in AGN?

Tim Waters[1],⋆ Daniel Proga[1], Randall Dannen[1], & Timothy R. Kallman[2]
[1]*Department of Physics & Astronomy, University of Nevada, Las Vegas, 4505 S. Maryland Pkwy, Las Vegas, NV, 89154-4002, USA*
[2]*NASA Goddard Space Flight Center, Code 662, Greenbelt, MD 20771, USA*

arXiv:1611.00407v2 [astro-ph.GA] 23 Jan 2017

Accepted XXX. Received YYY; in original form ZZZ

ABSTRACT

There is increasing evidence that the highly ionized multiphase components of AGN disc winds may be due to thermal instability. The ions responsible for forming the observed X-ray absorption lines may only exist in relatively cool clumps that can be identified with the so-called 'warm absorbers'. Here we calculate synthetic absorption lines for such warm absorbers from first principles by combining 2D hydrodynamic solutions of a two-phase medium with a dense grid of photoionization models to determine the detailed ionization structure of the gas. Our calculations reveal that cloud disruption, which leads to a highly complicated velocity field (i.e. a clumpy flow), will only mildly affect line shapes and strengths when the warm gas becomes highly mixed but not depleted. Prior to complete disruption, clouds which are optically thin to the driving UV resonance lines will cause absorption at an increasingly blueshifted line of sight velocity as they are accelerated. This behavior will imprint an identifiable signature on the line profile if warm absorbers are enshrouded in an even broader absorption line produced by a high column of intercloud gas. Interestingly, we show that it is possible to develop a spectral diagnostic for cloud acceleration by differencing the absorption components of a doublet line, a result which can be qualitatively understood using a simple partial covering model. Our calculations also permit us to comment on the spectral differences between cloud disruption and ionization changes driven by flux variability. Notably, cloud disruption offers another possibility for explaining absorption line variability.

Key words: line: formation, quasars: absorption lines, radiation: dynamics

1 INTRODUCTION

Many spectral properties of active galactic nuclei (AGN) are often explained by appealing to models involving high velocity clouds that can coexist with more highly ionized surrounding gas (for an overview see Krolik 1999 and Netzer 2013). However, the AGN environment is very hostile to such clouds because the strong radiation field and the presence of velocity shear leaves them prone to various hydrodynamical instabilities (e.g., Krolik 1977, 1979, 1988; Mathews & Blumenthal 1977; Mathews 1986). Therefore, for the clouds to be present, they either need to be confined or efficiently regenerated.

In a few recent papers we have addressed the issue of could formation and regeneration. In particular, in Proga et al. (2008) we presented results from global simulations of accretion flows irradiated by the AGN. We found these flows can turn into outflows due to radiation pressure. We also found that these outflows are clumpy due to thermal instability (TI; Field 1965) and the radiation force. In our subsequent papers we investigated the physics of these clouds in more detail using global simulations (Kurosawa & Proga 2008a; Barai et al. 2012; Moscibrodzka 2013) as well as local simulations (Proga et al. 2014; Proga & Waters 2015, hereafter PW15; Waters & Proga 2016, hereafter WP16). One of the main results of these studies is that TI and radiation pressure can facilitate the regeneration and acceleration of clouds.

In PW15 we showed how to self-consistently account for the increase in radiation force (due primarily to resonance line scattering) as a cloud forms and ion opacity increases. In so doing, we verified very early studies (e.g., Krolik 1977, 1979; Mathews & Blumenthal 1977) showing that radiatively accelerated planar clouds (i.e. 'slabs') are unstable to the Rayleigh-Taylor instability on the leading edge and will thus be disrupted. In WP16, we explored the effects of flux variability on the acceleration of clouds. We found that, independent of the presence of a variable flux,

⋆ E-mail: waterst3@unlv.nevada.edu

© 2016 The Authors

the gas remains two-phase and becomes highly mixed. The complicated velocity field supplies perturbations that permit the continual production of new clouds via TI, offsetting any losses to evaporation back into the hot medium. The long term state of the gas is a clumpy flow that accelerates at a nearly constant rate determined by the amplitude and frequency of the variations in the ionizing flux.

In this paper, we set out to calculate synthetic absorption line profiles for the simulations of PW15 and WP16, which probe a temperature regime appropriate for modeling warm absorbers. In particular, we sought to answer the following questions: (1) is it possible to differentiate, spectroscopically, between an ideal, comoving cloud (i.e. of planar or round geometry), a cloud being disrupted as it accelerates through its surrounding medium, and a completely chaotic, clumpy flow?; (2) can absorption line variability due to cloud disruption be distinguished from that due to variability in the ionizing flux? (3) can a standard partial covering analysis of our synthetic line profiles adequately reproduce the properties (namely, the velocity-dependent optical depth and covering fraction profiles) of our solutions?

As for the first question, our expectation is that cloud acceleration can in principle leave an absorption signature as the cloud is being disrupted, provided the absorption line is broader than the thermal width of the warm gas alone. Namely, the clumps of gas with the highest opacity end up the fastest moving, so that if absorption from warm gas is overall enshrouded in a broader absorption line formed in the hot inter-cloud gas, there will be systematically more absorption on the blue side of line center. Hence, the expected signature for the acceleration of a newly formed cloud is an initially symmetric line profile that becomes asymmetric with time as a somewhat deeper absorption feature (that tracks the warm cloud material) becomes increasingly blueshifted.

To confirm this expectation and answer the other questions posed, it was necessary to perform photoionization calculations in order to calculate line opacities for the most abundant ions present at the temperature range of our simulations. These calculations are described in §2, along with our methods for calculating simulated absorption lines. Our results are presented in §3, followed by our discussion in §4 and conclusions in §5.

2 METHODS

Time-dependent, 2D hydrodynamical simulations of a two phase medium form the basis for our calculations of absorption line profiles from first principles, as they provide the density, velocity, and temperature fields of the gas. This information is used to determine the opacity (and hence optical depth) of a specific ion by also running a dense grid of photoionization models using XSTAR (Kallman & Bautista 2001) for an assumed set of atomic abundances and spectral energy distribution (SED). The absorption line profiles are calculated by accounting for the attenuation of a uniform background source. Below we describe these methods in detail, emphasizing the underlying physical assumptions made when applying photoionization modeling to dynamical flow solutions. Finally, we discuss our procedure for making a comparison between our synthetic line profiles and a commonly used partial covering model (e.g., Barlow & Sargent 1997; Hamann et al. 1997).

2.1 Hydrodynamical simulations

Using ATHENA (Stone et al. 2008), we perform local cloud simulations similar to those presented in PW15 and WP16. These calculations account for many of the relevant microphysical processes believed to be important in the environment of AGN: heating and cooling due to the dominant radiative processes (photoionization and recombination, line cooling, bremsstrahlung, and compton/inverse compton processes using the formula from Blondin (1994)), thermal conductivity between the cloud and the inter-cloud medium, and a radiation force self-consistently determined from the heating processes and the number of lines present at a given temperature. Specifically, the radiative driving term was specified using the modified Castor, Abbot, & Klein (1975) method of Owocki et al. (1988), with a reduction of the force multiplier due to strong photoionization as computed by Stevens & Kallman (1990) and Kallman (2006, private communication), who also included a more realistic distribution of driving lines.

We focus our analysis on two different initial configurations leading to a clumpy medium: (i) a round cloud and (ii) a 'slab' configuration, which can be viewed as a local portion of a spherically symmetric shell of cloud material. Both configurations are arrived at by evolving a small isobaric perturbation in a homogenous, periodic box of nearly fully ionized gas that is thermally unstable.

For the purpose of this paper we run new simulations that are basically reruns of those presented in PW15. The main differences are that we use a square domain and for case (i) we take the amplitudes and growth rates of the initial perturbations to be identical in both the x and y directions to promote the formation of a round cloud.

For each configuration, we also carry out an additional simulation that uses a time-varying ionizing flux, $F_{\rm ion}(t)$, in order to study the effects of variability. This time dependence carries over to the photoionization parameter, $\xi = 4\pi F_{\rm ion}/n$, where n is the gas number density. As in WP16, we model the variability using a simple sinusoidal flux,

$$F_{\rm ion}(t) = F_X(1 + A_X \sin(2\pi t/t_X)), \quad (1)$$

where A_X and t_X are the amplitude and period of flux oscillations about a mean flux $F_X = n_{eq}\xi_{eq}/4\pi \approx 7.82 \times 10^8$ erg s^{-1} cm^{-2}. The subscript 'eq' denotes values used to define the initial equilibrium state of the gas. As described by PW15, $\xi_{eq} = 190$ is chosen based on numerical requirements to adequately resolve the interfaces between warm and hot gas. The relation $n_{eq}T_{eq} = 10^{13}$ cm^{-3} K typical of AGN (e.g., Krolik 1999) sets n_{eq} because $T_{eq} = 1.93 \times 10^5$ K is fixed by the radiative equilibrium curve once ξ is chosen (see PW15). We again adopt $A_X = 0.2$ and $t_X = 5\,t_{th} \approx$ 3.5 days, where $t_{\rm th}$ is the thermal time, defined as the ratio of the internal energy density of the gas to the net volumetric heating rate on the radiative equilibrium curve at (ξ_{eq}, T_{eq}).

These simulations explored a parameter regime chosen such that the majority of lines contributing to the line driving are optically thin. The gas is therefore too highly ionized to host an abundance of ions responsible for forming broad

absorption lines (BALs) commonly observed in the UV (e.g., S IV, C IV, O VI). The strongest line, as determined by our photoionization calculations described below, is the X-ray resonance line O VIII Lyα, which is a doublet with transitions at 18.9671 Å and 18.9725 Å. Our results are therefore confined to calculations for this line, commonly observed in warm absorbers (e.g., Turner & Miller 2009).

Warm absorbers are observed to have outflow velocities exceeding 100 km s^{-1} (e.g., Crenshaw et al. 2003). Our cloud simulations are local, meaning they are performed in the comoving frame of the cloud and therefore apply to warm absorbers formed at any velocity, so long as it is not relativistically large. We calculate line profiles as seen by a distant observer, and at time zero before the cloud is formed, we center the line profiles at zero velocity without loss of generality.

2.2 Photoionization calculations

Determining the detailed photoionization structure of our clumpy medium requires solving for, at every location in our domain, the fractional ion abundances and steady state level populations for a given set of elemental abundances. For this, we employ version 2.35 of the public code XSTAR (Kallman & Bautista 2001). XSTAR was run in constant density mode with $n_{\rm xstar} = 10^{10}$ cm^{-3}. To be consistent with the heating and cooling rates adopted in our cloud simulations, we used a 10 keV Bremsstrahlung SED. We assigned solar elemental abundances from Grevesse, Noels & Sauval (1996).

XSTAR calculates photoionization equilibrium, accounting for over 200,000 lines (Bautista & Kallman 2001), for gas with a given photoionization parameter and temperature. In our simulation domain, every grid cell is characterized by the two parameters (ξ, T) local to this cell. We therefore ran a grid of models in (ξ, T)-space covering the full parameter space of our solutions. This grid spanned 200 points logarithmically spaced over the range $\log\xi = 0$ to $\log\xi = 8$, and 94 points logarithmically spaced from $T = 5\times10^3$ K to 10^8 K. Since ATHENA has already determined the temperature of the gas, XSTAR is run with the option set to keep the input temperature fixed. XSTAR provides, in addition to the ionization structure, quantities such as the opacity, emissivity, excitation and dexcitation rates, and heating/cooling rates due to individual processes.

The relevant value we extract from XSTAR is the comoving frame line center opacity of a resonance line (uncorrected for stimulated emission),

$$\begin{aligned}\kappa_{\nu_0} &= \frac{\pi e^2}{m_e c}\frac{n_1}{\rho} f_{12}\,\phi(\nu_0) \\ &= \frac{1}{\sqrt{\pi}}\left(\frac{\pi e^2}{m_e c}\frac{A\,n_{\rm xstar}}{\nu_0 (v_{th}/c)} f_{12}\,\eta_{ion}\right).\frac{1}{\mu m_p n_{\rm xstar}}.\end{aligned} \quad (2)$$

Here, $\rho = \mu m_p n$ is the hydrodynamic density (we set $\mu = 1$ in this work), f_{12} is the oscillator strength of the lower level of the line, n_1 is the level population of the ion's ground state, and $\phi(\nu)$ is the line profile that will be calculated separately (see §2.3). The level population is related to the number density from our hydrodynamical solutions through $n_1 = A\,\eta_{\rm ion}\,n$, where A is the elemental abundance relative to hydrogen and $\eta_{\rm ion}$ is the fractional ion abundance. In the second line, $v_{th} = \sqrt{2\,k\,T/m_{\rm i}}$ is the mean thermal velocity of an ion with atomic weight $m_{\rm i}$. The term in parenthesis is the attenuation coefficient we extract from XSTAR. In the remaining term, we correct for the constant density assigned to XSTAR, $n_{\rm xstar}$. By applying the density correction in this way, we assume that the opacity is rather insensitive to n, depending instead on the ratio of the density of photons to the gas number density, i.e. the photoionization parameter. Given ξ and T, we determine the line center opacity from XSTAR output using a lookup table that bilinearly interpolates between the values in our grid.

Table 1. Characteristic recombination rates and comparison with dynamical timescales for three representative XSTAR models.

Gas regime (T [K], ξ [ergs cm s^{-1}])	Atom/ Ion	$n_e\alpha$ [s^{-1}]	$t_{\rm dyn}/t_{\rm rec}$
Warm	H I	1.04×10^{-3}	1.1×10^{2}
$(7.53\times10^4, 77.0)$	O VIII	1.21×10^{-1}	1.2×10^{4}
Evaporating	H I	4.45×10^{-4}	5.0
$(1.93\times10^5, 190.0)$	O VIII	7.64×10^{-2}	8.6×10^{2}
Hot	H I	1.87×10^{-4}	8.6
$(4.77\times10^5, 475.0)$	O VIII	4.56×10^{-2}	2.1×10^{3}

The shortest timescale on which clouds can undergo structural changes is the sound crossing time across a layer of cloud material. The thinnest cloud layers in our simulations belong to clouds about to undergo evaporation, which occurs on a longer timescale; the length scale for evaporation therefore determines the smallest cloud sound crossing time. This length scale is the Field length, $\lambda_F = 2\pi\sqrt{\kappa T/\rho\Gamma}$ (Begelman & McKee 1990), giving $t_{\rm dyn} = \lambda_F/c_s = 2\pi\sqrt{\kappa/(\gamma n k\Gamma)} \approx 10^4\,n_8^{-1/2}$ s, where n_8 is the number density in units of 10^8 cm^{-3} and we have plugged in fiducial values for the thermal conductivity κ and the volumetric heating rate Γ on our radiative equilibrium curve at $\xi = 190$ (see PW15). Note that this time-scale is still sensitive to temperature since both κ and Γ have implicit temperature dependence. We must compare $t_{\rm dyn}$ with the recombination time-scale, $t_{\rm rec}$, as it is the microphysical process that typically has the longest time-scale (e.g., Ferland 1979).

Recombination rates per ion, $n_e\alpha$ (where n_e is the free electron number density), as well as the ratios $t_{\rm dyn}/t_{\rm rec}$ for both hydrogen and O VIII are tabulated for three different temperatures and corresponding photoionization parameters in Table 1. The middle row was calculated for (T_{eq}, ξ_{eq}), the equilibrium values used to set the initial conditions of the simulations, and these values are characteristic of those for the evaporating gas. The top and bottom rows quote values for T and ξ typical of the warm and hot gas in the domain at any given time as the gas evolves. For this gas, the dynamical

time is defined as simply the domain sound crossing time, L_x/c_s (at the appropriate sound speed). We see that the necessary condition $t_{\rm dyn} > t_{\rm rec} \equiv (n_e\alpha)^{-1}$ is always satisfied by at least a factor of 5 for hydrogen. Thus, the validity of applying photoionization calculations to calculate the ionization structure of our dynamical flow solutions has been established, even for the most transient, evaporating gas in our simulations.

2.3 Absorption line profiles

A formal solution of the radiative transfer equation that holds when the source function for local emission is zero reads

$$\mathscr{L}_\nu = \int_0^{L_y}\int_0^{L_x} \mathcal{I}_\nu(x,y) e^{-\tau_\nu(x,y)} dx\, dy, \tag{3}$$

where $\mathcal{I}_\nu(x,y)$ is the monochromatic specific intensity of the background source. This integral is taken over an imaginary plane of the sky (located beyond the absorber) of linear dimensions (L_x, L_y) as viewed by a distant observer, while evaluating the optical depth $\tau_\nu(x,y) = \int \kappa_\nu \rho\, dz$ requires an integration of the opacity $\kappa_\nu(x,y,z)$ over the line of sight (LOS) coordinate z. Note that by neglecting the source function, we do not account for scattering and remission of the line photons. Therefore, we do not include certain effects such as the net expansion of the medium, which can allow photons to be first absorbed in the blue component, and then reemitted and absorbed by the red component in a different region of the flow (e.g., Castor and Lamers 1979).

The calculation of absorption lines simplifies when there is symmetry along the y-direction of the observer plane, the case for 2D simulations. Integrating over y and measuring x in units of $L_x = 3.1\times10^{11}$ cm so that x varies from 0 to 1 gives

$$\mathscr{L}_\nu = L_x\, L_y \int_0^1 \mathcal{I}_\nu(x) e^{-\tau_\nu(x)} dx, \tag{4}$$

where now the x-coordinate defines a single LOS in our calculations. We assume that the background intensity is constant. Thus, by defining the normalized absorption line profile $I \equiv \mathscr{L}_\nu/(L_x\, L_y\, \mathcal{I}_\nu)$, we arrive at

$$I(\nu) = \int_0^1 e^{-\tau_\nu(x)} dx. \tag{5}$$

Evaluating the optical depth requires calculating the opacity $\kappa_\nu(x,z) = \kappa_{\nu_0}(x,z)\phi(\nu)/\phi(\nu_0)$ at every location in the domain. As described in §2.2, we directly determine κ_{ν_0} from XSTAR. The line profile function $\phi(\nu)$ is evaluated separately using our hydrodynamical variables. Every finite volume cell in our grid-based solution is treated as a parcel of gas that is thermally broadened according to its cell-centered temperature (between about 2×10^5K and 10^6K) and Doppler shifted away from line center according to its LOS velocity. Each local line profile is then specified as a Gaussian,

$$\phi(\nu) = \frac{1}{\sqrt{\pi}}\frac{1}{\Delta\nu_0}\exp\left(\frac{-(\nu-\nu_D)^2}{\Delta\nu_0^2}\right), \tag{6}$$

where $\Delta\nu_0 = \nu_0 v_{th}/c$ is the thermal linewidth and $\nu_D = \nu_0(1+v_z/c)$ is the Doppler shifted frequency at line center. We note that the width of the resulting net line profile is primarily set by the thermal velocity of the hot gas, $v_{th,hot} \approx 20-25$ km s^{-1}, but it can also be increased by the z-component of the local velocity field.

We use the trapezoidal rule to evaluate both the optical depth integral and the integral in equation (5) numerically. These integrations are performed at 150 different frequencies centered around ν_D. In practice, we work in velocity space, binning the range $[v_c - 50$ km s^{-1}, v$_{\rm c}$ + 50 km s$^{-1}]$, where v_c is the 'cloud-tracking' velocity, or the velocity of the comoving frame that is used by ATHENA to keep the cloud centered on the domain.

2.4 Doublet lines and the PPC model

As mentioned, we apply the above methods to simulate absorption from O VIII Lyα, a common X-ray doublet line, whose synthetic line profiles will be denoted I_r and I_b. The subscripts 'r' and 'b' distinguish these doublet components, with I_b having a slightly higher (bluer) frequency. Many doublet lines have the property that the stronger line has an oscillator strength almost exactly twice that of the weaker line (due to relativistic effects, the fractional difference is $\sim 10^{-4}$), and so the ratio of line-center opacities is also almost 2.

Doublet lines produced in a clumpy medium are especially interesting, as revealed by the so-called pure partial covering (PPC) model (Barlow & Sargent 1997; Hamann et al. 1997; de Kool et al. 2002), a widely used model for estimating the ionic column densities of AGN outflows (e.g., Crenshaw et al. 2003). According to this model, the absorption line profiles for the two transitions are

$$\begin{aligned} I_r &= (1-C_\nu) + C_\nu\, e^{-\tau_{\nu,r}};\\ I_b &= (1-C_\nu) + C_\nu\, e^{-2\,\tau_{\nu,r}}. \end{aligned} \tag{7}$$

These expressions follow from equation (5) when the spatial distribution of optical depth along the LOS consists of some fraction $(1-C_\nu)$ of purely optically thin gas with $\tau_\nu = 0$, with the remaining gas optically thick with constant $\tau_\nu (= \tau_{\nu,r}$ for $I_r)$, giving an unambiguous definition of the LOS covering fraction, C_ν. The PPC model reveals that any differences between the profiles I_b and I_r^2 are due to partial covering ($C_\nu < 1$), and therefore doublet lines encode information about the distribution and optical depth of clouds. As we will show, they can also be used to infer the presence of cloud acceleration.

We will invoke the PPC model to help interpret our results, so for consistency we should compare the properties of our simulations to this model's 'doublet solution', i.e. its predictions for C_ν and $\tau_{\nu,r}$ when applied to our synthetic doublet lines, I_r and I_b. We must therefore calculate the covering fraction C_ν and a mean value of the optical depth, $\overline{\tau}_\nu$ from our simulations. To define either quantity, we require an operational definition of obscuration, i.e. a cutoff optical depth value, $\tau_{\rm cut}$, above which the background source is considered 'covered'. The fraction of sight lines with $\tau_\nu(x) > \tau_{\rm cut}$ defines C_ν, while the average of $\tau_\nu(x)$ above this cutoff defines $\overline{\tau}_\nu$:

$$\begin{aligned} C_\nu &= \int_0^1 H[\tau_\nu(x) - \tau_{\rm cut}]\, dx,\\ \overline{\tau}_\nu &= C_\nu^{-1}\int_0^1 \tau_\nu(x) H[\tau_\nu(x) - \tau_{\rm cut}]\, dx. \end{aligned} \tag{8}$$

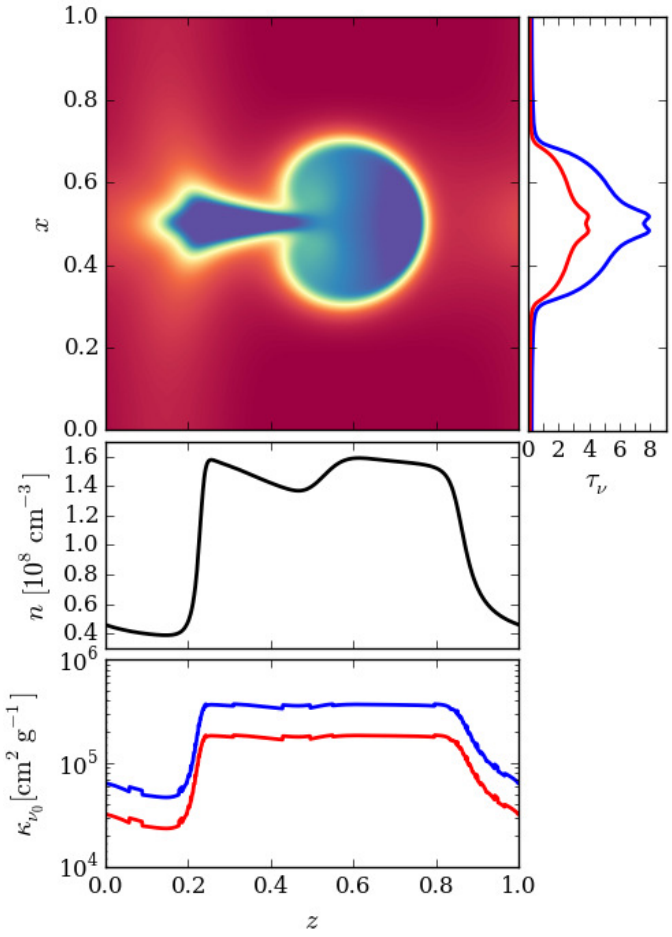

Figure 1. Illustrative calculation of the optical depth at line center, $\tau_{\nu_0}(x)$. The top row shows an image of the density field and the resulting spatial profile of $\tau_{\nu_0}(x)$. Both the x and z dimensions are measured in units of $L_x = 3.1 \times 10^{11}$ cm. We plot profiles of $\kappa_{\nu_0}(z)$ through the center of the domain ($x = 0.5$) for each component of the doublet in the bottom panel. This quantity has been extracted from XSTAR using a lookup table based on the values of (ξ, T), where ξ is calculated from n, plotted in the middle panel.

Here, $H(x)$ is the Heaviside step function. Note that these equations demand the profile $\tau_\nu(x)$ to be monotonically increasing. Provided the physical source is unresolved, so that an observer measures the integrated flux, $\tau_\nu(x)$ can always be sorted prior to integration.

3 RESULTS

To illustrate our procedure for calculating simulated line doublets, in Figure 1 we display the relevant quantities that enter our calculations. The top panel shows a 2D image of the number density along with an adjacent plot displaying the optical depth profiles of the two doublet lines along the x-axis. Here, $\tau_\nu(x)$ has been calculated at line center. We will always take 'line center' to mean at $v = -v_c$ in velocity space, corresponding to frequencies near $\nu_D = \nu_0(1 + v_z/c)$ in frequency space. The bottom panel shows sample profiles of $\kappa_{\nu_D}(z)$ for each transition along a horizontal slice through the center of the domain. This profile, in turn, is calculated from the profiles of density and temperature, and density is shown in the middle panel. Notice that for this snapshot, the density only varies by a factor of 4 between warm and hot gas (as does temperature), while the line center opacity varies by a factor of about 60. This indicates that the ion fraction, $\eta_{\rm ion}$, is highly sensitive to the physical conditions of the gas.

To compute the emergent flux at this line center frequency, we first attenuate a uniform background source according to these optical depth distributions. A distant observer will measure this attenuated flux integrated over x. To construct the profiles I_r and I_b, we simply perform this integration and then repeat this procedure for all frequency bins.

Note that because our domain size, $L_x = 3.1 \times 10^{11}$ cm, is typically much less than the characteristic scale of an X-ray source ($R_X \sim 10^{13}$ cm for a Seyfert galaxy with a black hole mass $10^7 \mathrm{M}_\odot$), we are implicitly assuming a global covering fraction of clouds similar to the local covering fraction of warm gas in our domain. That is, in order for our calculations over a single domain to carry over to the full extent of the continuum source, we must envision an ensemble of $\sim (R_X/L_x)^2 \approx 10^3$ individual adjacent domains, each containing an evolving cloud. Interpreted in terms of the cloud formation mechanism described in PW15, such a large number of clouds requires only the existence of an SED that can give rise to a thermally unstable region surrounding the continuum source. Any number of perturbations can grow simply through a large change in ionizing flux triggering cloud formation at a wavenumber, $k_{\rm max}$, corresponding to the maximum linear growth rate of the TI; $L_x = 2\pi/k_{\rm max}$ was assigned based on this characteristic length scale (see PW15). Due to the existence of this length scale, the distributions of resulting cloud sizes and densities are likely to be sharply peaked about some characteristic values that are only a function of the SED and photoionization parameter. We therefore would not expect the basic results presented here to change if this 'global' problem were to be directly modeled.

3.1 Synthetic absorption lines

The results of our line profile calculations are presented in Figures 2 and 3, where we show the time evolution of our two cloud configurations with and without a time-variable ionizing flux. The leftmost panels in either figure are the same, as the variable flux is not applied before this time. Each frame is separated by a half period ($t_X/2$) of the sinusoidal flux cycle, about 1.8 days (see §2.1). The velocity field of the gas is decomposed as $\vec{v}(x,z) = \delta v_x(x,z)\hat{x} + [v_c + \delta v_z(x,z)]\hat{z}$, where v_c is the velocity of the comoving frame that defines 'line center' and $(\delta v_x, \delta v_z)$ denotes the local velocity field, whose directionality is depicted by the arrows, with the light grey to black color gradient representing the transition from negative to positive δv_z. We display v_c on the upper left corner of each panel in km s^{-1}, whereas the bracketed numbers in the bottom of each panel summarize the local LOS velocities: the left (right) number is the average over all velocities with $\delta v_z < 0$ ($\delta v_z > 0$). The bottom rows of panels display the corresponding synthetic absorption lines for the O VIII doublet.

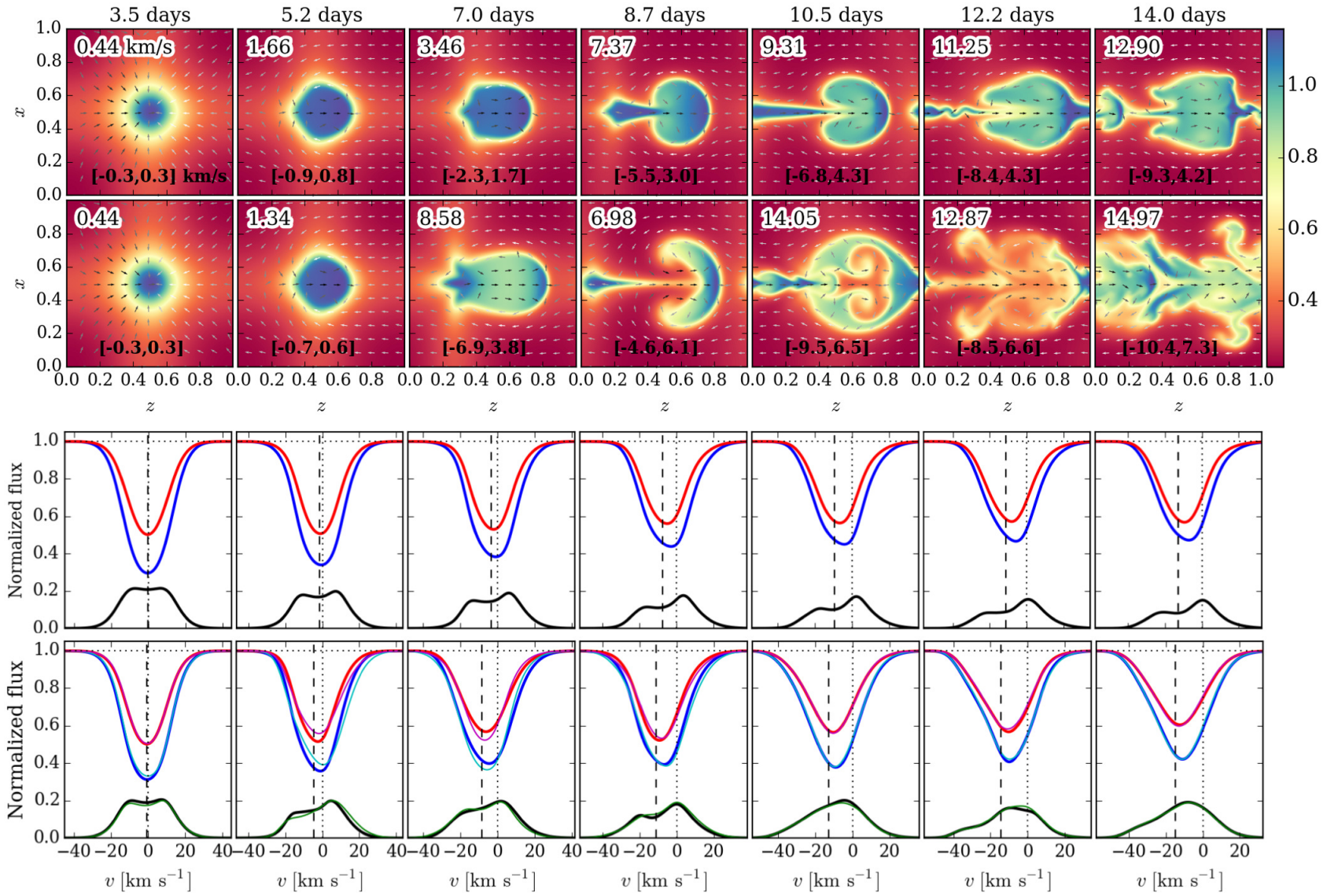

Figure 2. Densiy maps (colorbar shows number density, n, in units of 10^8 cm^{-3}) and corresponding synthetic absorption line profiles for a constant flux run (first row of panels) and a variable flux run (second row of panels). The early cloud formation stage is not shown. The source of radiation is plane parallel and emanates from the left (at $z = -\infty$), while the observer is to the right (at $z = \infty$). The numbers in the top left of every density panel are the comoving velocities of the cloud, v_c, in km s^{-1} and correspond to the vertical dashed lines in the bottom rows. Arrows on the density maps depict the local velocity field, with the gradient in colors from light grey to black representing the transition from negative to positive local LOS velocities, δv_z. The numbers in the brackets denote averages over all $\delta v_z < 0$ and $\delta v_z > 0$. Blue and red lines denote I_b and I_r, the stronger and weaker lines of the O VIII doublet, while the black lines show the difference $I_r - I_b$. To assess the line variability for the variable flux run, we overplot I_b, I_r, and $I_r - I_b$ using cyan, magenta, and green lines, respectively, for line profiles calculated at the later time $t + t_X/4$, which is either a high or low flux state; the density maps are always shown for a mean flux state. A partial covering analysis reveals that $I_r - I_b \approx C_\nu e^{-\tau_\nu}$, so dips in this profile can be caused by gas with higher optical depth, leading to the appearance of humps. The location of the dip tracks the faster moving, more opaque cloud material.

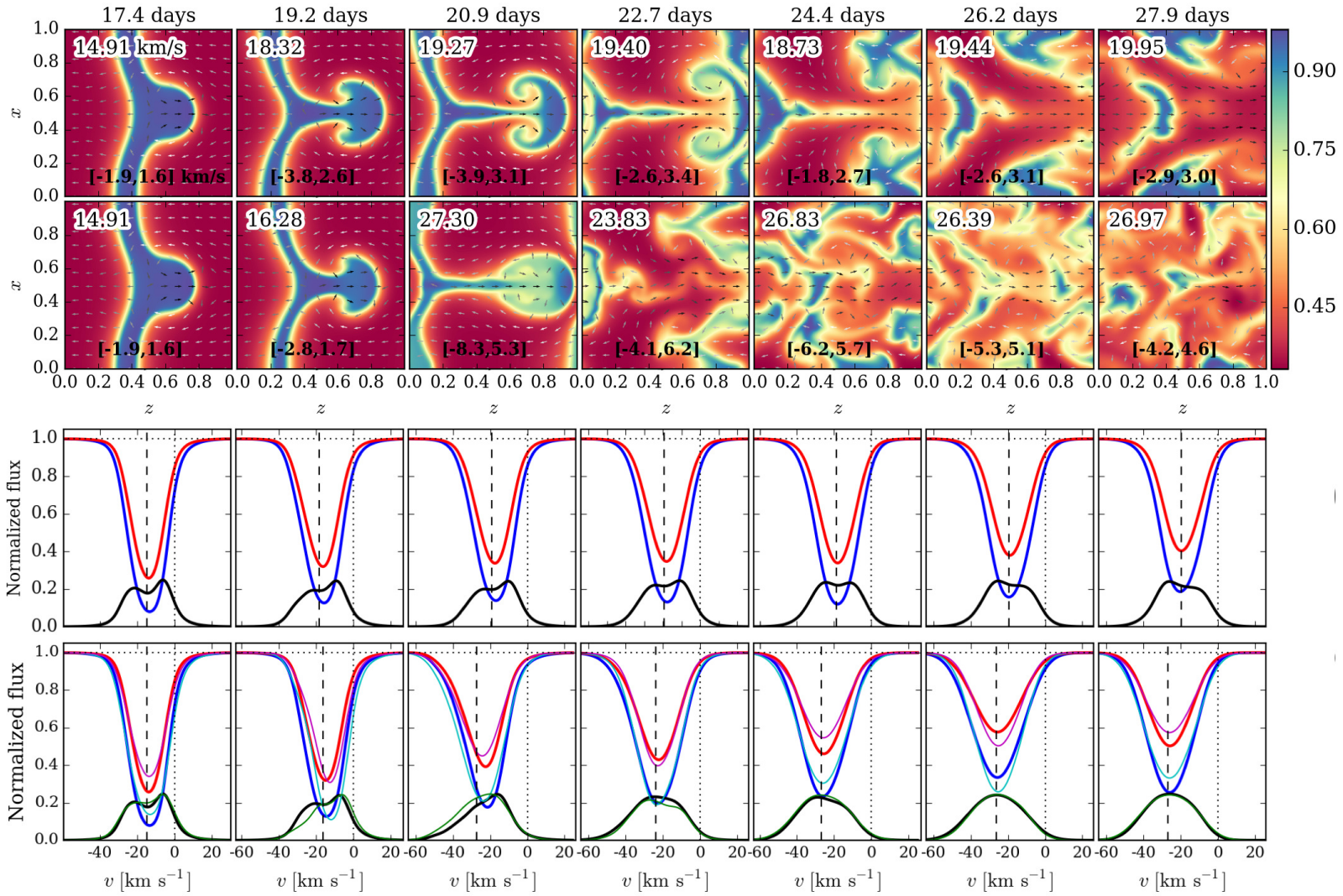

Figure 3. Same is Figure 2 but for the slab geometry. Compared to the round cloud case, there is less rapid acceleration and therefore the deeper absorption expected on the blue side side of line center is not actually visible on the line profiles. However, the diagnostic $I_r - I_b$ still reveals the presence of large differences in the local velocity field. Notice that in the bottom panels this signature of cloud acceleration gets wiped out as the cloud is disrupted since the velocities of the clumps become randomized.

Our main result is that the absorption lines are overall smooth and nearly featureless, despite the dramatic changes in cloud morphology. The reason for this is that the temperature distribution of the gas is the dominant factor in determining line shapes, as cloud acceleration and disruption does not generate enough velocity dispersion to significantly impact the line shapes. As indicated on the density images, the difference between the mean positive and negative LOS velocities increases with time, reaching $10-15$ km s^{-1} in Figure 2 and $5-10$ km s^{-1} in Figure 3. These relative velocities do not exceed the thermal velocity for O VIII in the hot gas, which is about 20 km s^{-1}. Thus, Doppler shifts due to the bulk velocities have a sub-dominant effect on the line widths.

However, for the round cloud case the velocity dispersion due to cloud acceleration does exceed the thermal velocity for O VIII in the *warm* gas, which is about 10 km s^{-1}. Such systematic differences in velocity can viewed as velocity-space inhomogeneities in optical depth and visibly manifest as an asymmetry on the line profiles, as can be seen in Figure 2. Beginning with the third panel, the blue line profiles develop an asymmetry, showing deeper absorption to the left of line center, which is the expected signature for cloud acceleration as explained in the introduction.

Nevertheless, this asymmetry is admittedly subtle and moreover its presence is barely apparent for the slab geometry in Figure 3. Comparing the velocities from one frame to the next in Figure 3, it is clear that the bulk flow acceleration is substantially less compared to those in Figure 2, explaining the lack of a noticeable acceleration signature. It is nevertheless possible to reveal its presence, as we now proceed to show.

3.2 A spectral diagnostic for cloud acceleration

Our analysis reveals that the difference $I_r - I_b$ leads to a profile whose shape is a sensitive diagnostic of cloud acceleration. This quantity is plotted in black in the lower panels of Figures 2 and 3. To assess the degree of variability, this quantity is also plotted in green in the bottommost row for a snapshot displaced in time a quarter cycle ($t_X/4$) ahead of that shown in the image, corresponding to a high or low flux state. Notice the overall trend among all cases: the profile for $I_r - I_b$ shows prominent asymmetric double humps when clouds are being accelerated, while the humps are small or altogether absent once the cloud is fully disrupted. Importantly, these features are nearly as prominent in Figure 3 as they are in Figure 2, despite the line profiles for the slab configuration being visibly symmetric and therefore lacking an obvious signature for cloud acceleration.

To explain these features, we have marked the values of v_c with black dashed vertical lines, showing that they intersect the dips in $I_r - I_b$. Evidently these dips track the accelerating cloud and in turn lead to the appearance of humps. Notice that these vertical lines are to the left of the locations of $\min(I_r)$ in Figure 2, implying that there is less residual flux at the blueshifted velocity v_c compared to the same offset to the right of $\min(I_r)$, in agreement with our expectations.

A qualitative understanding of the behavior of $I_r - I_b$ can be gained with the help of the PPC model. From equation (7), we have

$$\begin{aligned} I_r - I_b &= C_\nu e^{-\tau_{\nu,r}}(1 - e^{-\tau_{\nu,r}}), \\ &\approx \begin{cases} C_\nu e^{-\tau_{\nu,r}} & \text{(near line center);} \\ \tau_\nu C_\nu e^{-\tau_{\nu,r}} & \text{(in the line wings).} \end{cases} \end{aligned} \tag{9}$$

We invariably find C_ν to have a flat or mildly increasing slope near line center (see §3.3). Hence, the only way for the profile of $I_r - I_b$ to lose monotonicity near line center is if there are velocity-space inhomogeneities in τ_ν. In other words, on the basis of the PPC model, a fast moving clump should indeed carve out a blueshifted dip in the otherwise smooth profile of $I_r - I_b$.

Note, however, that v_c does not always become increasingly blueshifted with time; in Figure 3, the vertical dashed lines can lie to the right of the velocity corresponding to $\min(I_r)$, indicative of locally redshifted cloud motion. To explain this occurrence and verify quantitatively that the dips in $I_r - I_b$ are always tracking the mean cloud motion, we extract gas properties only along sight lines for which $\tau_\nu(x) > 1$ (at a velocity corresponding to $\min(I_b)$) to exclude sight lines with only hot gas. This will eliminate $\sim 1/3-1/2$ of all x-values in Figure 2 but few or no sight lines in Figure 3. Within this subset of our domain, we then determine the average velocity and mass fraction of the warm ($T < T_{eq}$) and hot ($T > T_{eq}$) gas.

In the top panel of Figure 4, we plot these quantities versus time as solid blue and red curves, along with v_c (dashed black line) and the velocities corresponding to the locations of $\min(I_r)$ and $\min(I_b)$ (dashed red and blue lines, respectively). For the round cloud case, we find a clear separation in velocities between warm and hot gas, with the average velocity of warm gas at all times exceeding those marking $\min(I_r)$ and $\min(I_b)$. It also nicely traces the curve of v_c, which is a consistency check since v_c was computed using a mass-weighted average over *all* warm gas in Athena. For the slab case, on the other hand, there is only a marginal separation in velocities between warm and hot gas until $t = 34t_{th}$, when the cloud material overall reverses direction. That is, it retains a net overall blueshift according to the total LOS velocity $v_z = v_c + \delta v_z$, but the local LOS velocity δv_z becomes (on average) negative. This occurrence corresponds the last 3 panels in Figure 3, where it is clear that the clump in the center of the domain still has $\delta v_z > 0$, but the larger clumps at the top and bottom of the domain have $\delta v_z < 0$. This sign change of the local LOS velocity is reflected in the profile of $I_r - I_b$, as the absorption dip tracing the warm gas shifts from the left side of $\min(I_r)$ to the right side.

In the lower panels of Figure 4, the higher mass fraction of warm gas indicates that the shape of the line profiles should primarily be controlled by the dynamics of the cloud. We can then ask why, since the warm gas is closely tracked by the speed v_c, are the line profiles not more sharply peaked around the dashed black vertical lines marking v_c? The answer is that there is significant absorption in both the evaporating gas component (yellow colors in Figures 2 and 3) and the hot gas (red colors), so that the cloud is overall enshrouded in a background absorption profile. We will return to this point below, as it implies that the hot gas has non-negligible optical depth, which is at odds with a basic assumption of the PPC model.

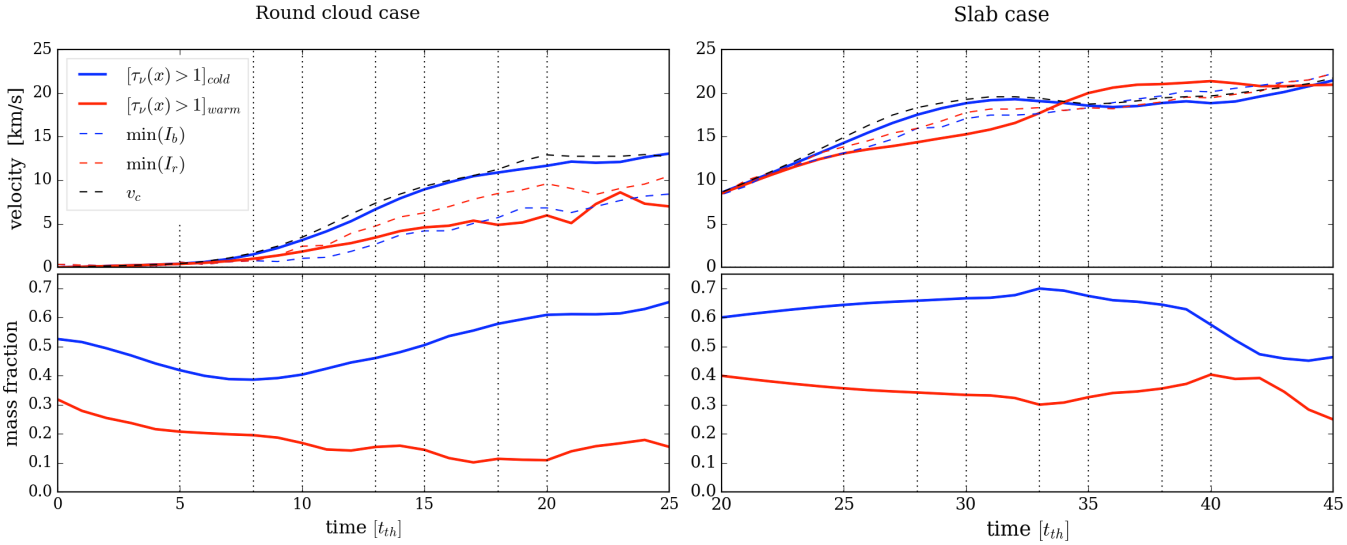

Figure 4. Temporal analysis linking cloud acceleration with the expected absorption properties. The dotted vertical lines mark times corresponding to the snapshots in Figures 2 and 3. The thick solid red and blue curves denote the velocity (top panels) and mass fractions (bottom panels) averaged only along sight lines with high optical depth (i.e. only for x with $\tau_\nu(x) > 1$). The dashed red and blue lines trace the locations of line center (the minima of I_r and I_b, respectively). The dashed black line marks v_c, the average velocity all warm gas in the domain, and corresponds to the dashed vertical lines in Figures 2 and 3. Since this curve coincides with the blue one, the dips in $I_r - I_b$ indeed trace the motion of cloud. In Figure 3 the center of these dips move to the right of min I_r, which is shown more clearly here as the blue line pass beneath the red in the right panel, indicating that the cloud is moving slower than its surroundings on average.

3.3 Partial covering analysis

We have already invoked the PPC model to qualitatively explain the behavior of the profile $I_r - I_b$. Here we examine the predictions of this model more closely, by comparing our results against its 'doublet solution', obtained by solving equation (7) for $\tau_{\nu,r}$ and C_ν:

$$\tau_{\nu,r} = -\ln I_r - \ln\left[\frac{I_r - I_b}{I_r - I_r^2}\right], \qquad C_\nu = \frac{1}{1 + (I_b - I_r^2)/(1 - I_r)^2}. \tag{10}$$

These expressions are equivalent to those quoted in the literature (c.f. Arav, Korista, & de Kool 2002), but the first now explicitly shows the 'correction' to $-\ln I_r$, the prediction for $\tau_{\nu,r}$ in the case of no partial covering (when $I_b = I_r^2$). It reveals the upper bound $I_b \leq I_r$, since obviously we must have $I_r > I_r^2$. Meanwhile, the second expression immediately gives the lower bound $I_b \geq I_r^2$, because $C_\nu \leq 1$ by definition, with $C_\nu = 1$ corresponding to $I_b = I_r^2$ as required. Thus, the behavior of these expressions as a function of I_b and I_r is evident: the larger the difference between I_b and I_r^2, the smaller the covering fraction and the larger the correction for the 'true' optical depth of the absorber.

However, whenever $I_b \to I_r$ the correction term to the optical depth will clearly blow up, and the profile for $\tau_{\nu,r}$ must therefore be truncated in the line wings when $I_r - I_b$ becomes very small. Only near line center is this behavior physical, for in the limiting case of doublets with matching residual intensities ($I_b = I_r$) and $\tau_{\nu,r} = \infty$, we correctly recover $C_\nu = 1 - I_r$, which is a lower bound on the profile for C_ν. In practice, application of the PPC model has typically been limited to the core of the line due to a similar anomalous effect causing unphysical values for C_ν upon attempting to deconvolve the line profiles with the instrument's line spread function (e.g., Ganguly et al. 1999; Hall et al. 2003).

In the PPC model, the spatial optical depth profile is a step function at each frequency, which entails the following assumptions: (i.) the hot gas has zero optical depth; (ii.) the warm gas has a single optical depth value (equal to $2\tau_{\nu,r}$ in the case of the stronger line of the doublet); and (iii.) the covering fractions of either line in the doublet are the same. We assess these assumptions at line center in Figure 5, by taking the spatial optical depth profile from Figure 1 as a case in point. In the top panel of Figure 5, we plot $\tau_\nu(x)$ on a log-scale, showing that its minimum value is about 0.25 for the blue component, which is hardly negligible. In the bottom panel, we sort $\tau_\nu(x)$ to make it a monotonically increasing profile. We see that it indeed can be crudely approximated as a step function, with $\tau_{\nu,r}$ being represented by $\overline{\tau}_\nu$ (marked with a red dashed line), computed using equation (8). Additionally, the separation between the two vertical dashed lines measures the difference in covering fractions of either component (see the caption for details). Since it is relatively small, we conclude that assumption (i) will be the most severe upon comparing the PPC model's doublet solution with our simulations. This comparison is carried out in the top two rows of Figure 6 for times corresponding to the first, middle, and last panels in Figure 2. We indeed find that the predictions of the PPC model, the black solid profiles, do not agree well with the exact values measured from our simulations. However, we confirm in Appendix A that the agreement can be improved by accounting for the fact that the hot gas has a non-negligible optical depth.

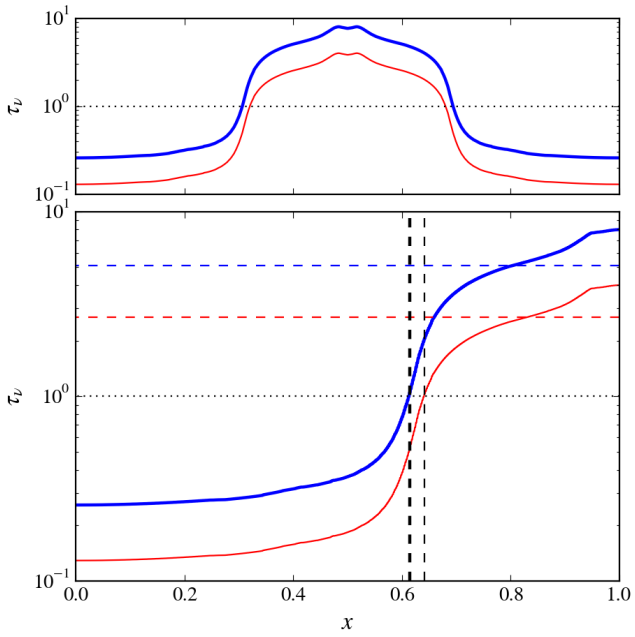

Figure 5. Method to calculate representative values of τ_ν and C_ν in order to assess the PPC model. The top panel reproduces the spatial optical depth profiles from Figure 1, but on a log-scale. In the bottom panel, we sort these profiles in order of increasing optical depth. We then apply equation (8), taking $\tau_{\nu,\rm cut} = 1$, which is marked by the dotted line. The blue and red horizontal lines show $\overline{\tau}_\nu$ for each transition, which is the average of $\tau_\nu(x)$ to the right of the thick and thin black vertical dashed lines, respectively. The location of these vertical lines define $1 - C_\nu$ at line center. Repeating this procedure at all frequencies, we arrive at the 'exact' values plotted as a function of velocity in Figure 6.

3.3.1 Effects of partial covering

Notice from Figure 6 that the peak of the optical depth profile does not coincide with $\max(C_\nu)$ or $\min(I_b)$ in the second and third panels. This is a partial covering effect: if we were to only calculate line profiles for sight lines in the middle half of the domain, this would not be the case. In other words, the line profile due to the warm gas alone is almost completely saturated, so the residual flux around v_c is coming entirely from the flux transmitted through the hot gas.

The cloud is still in the process of forming in the left panel, and therefore the warm and hot gas only differ in density and temperature by about a factor of 2. This is why I_b is approximately equal to I_r^2 in the bottom left panel, as the effects of partial covering are minimal in the absence of significant optical depth contrasts.

Another partial covering effect is the tail appearing on the blue side of the C_ν profiles in the middle and right panels. Since fast moving clumps tend to have higher C_ν, this is in agreement with expectations. We note that the PPC model's doublet solution, despite grossly overestimating the red side of C_ν, correctly captures this overall feature on the blue side.

3.4 Line profile variability

The blue and red line profiles in the last row of Figures 2 and 3 correspond to times in which the sine function is zero in equation (1). Overplotted with these are line profiles corresponding to the nearest high or low flux state (when $\sin(2\pi t/t_X) = \pm 1$) to show the effects of variability in response to changes in the ionizing flux. As shown by WP16, there are significant variations in temperature and density during these states, yet this evidently only amounts to a moderate level of flux variability. Comparing the strengths of the lines across each row, we see that more variability is caused by cloud disruption than by the response of the gas to the 20% changes in ΔF_X.

Indeed, comparing the cases without variability in the ionizing flux, we see that the time-dependent cloud dynamics alone causes significant absorption line variability. Furthermore, in an environment prone to TI, a large change in ΔF_X (i.e. $A_X \gtrsim 1$ in equation (1)) can trigger cloud formation by displacing ξ to unstable regions on the radiative equilibrium curve (PW15), and this original deepening of the line profile (not shown here) can also be a source of variability.

4 DISCUSSION

We have combined 2D hydrodynamic simulations of the evolution of irradiated, thermally unstable gas in AGN with a dense grid of XSTAR models in order to calculate the detailed photoionization structure of the gas. This type of calculation represents the state of the art, as several research groups have recently developed interfaces between a hydrodynamic code and either XSTAR (Kinch et al. 2016) or CLOUDY (Salz et al. 2015; Ramírez-Velasquez et al. 2016) in order to self-consistently account for radiation source terms under the assumption that photoionization equlibrium is established on time-scales short compared to all relevant dynamical time-scales (recall §2.2). Of these efforts, only Kinch et al. (2016) have also performed 2D simulations. Our approach here is not fully self-consistent, even within this approximation, as the heating and cooling rates and radiation force used in our hydrodynamic simulations are based on analytic fits to earlier photoionization calculations that assumed the same SED (see PW15 for details). Here, XSTAR output is not being coupled to the hydrodynamics, as that first requires a non-trivial calculation of the force multiplier resulting from a given SED, work which is underway in our group (Dannen, Proga, & Kallman 2016, in preparation). While we have yet to explore how different SEDs can affect the acceleration and dynamics of clouds, they are unlikely to change the qualitative outcome of our local cloud simulations, which show that the flow becomes turbulent but remains clumpy.

Several global models of the broad line region (BLR) exist in which cloud formation is attributed to TI. For example, Wang et al. (2012) considered a global model for episodic BLRs in which TI is ultimately responsible for the cloud production, with the origin of the gas being attributed to a Compton heated wind arising from the irradiated 'skin' of a self-gravitating accretion disc. Recently, Begelman & Silk (2016) proposed the idea of magnetically elevated accretion discs and showed that TI should operate in the uppermost layers of the disc, thereby providing a different candidate

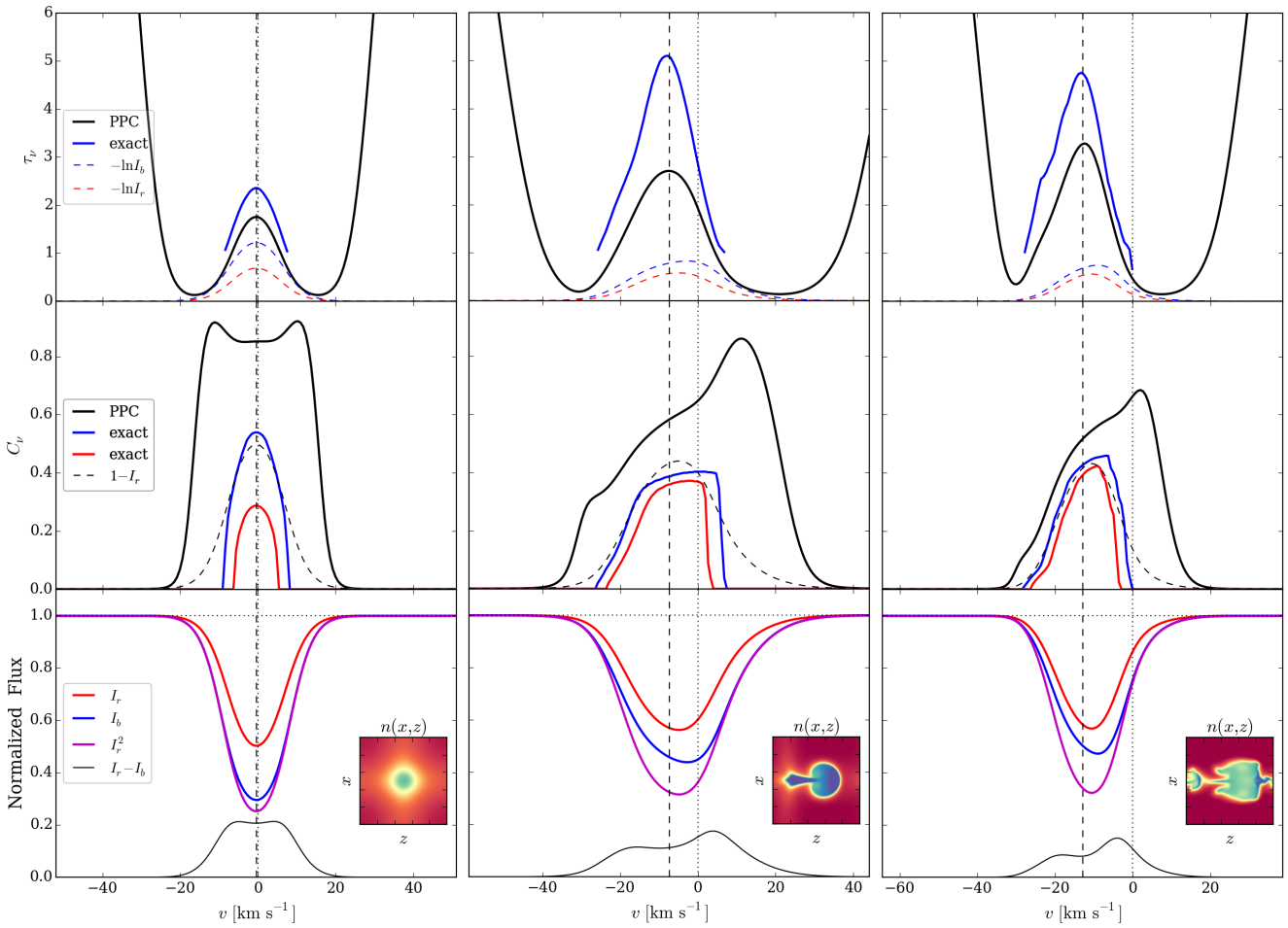

Figure 6. Comparison between the doublet solution of the PPC model (thick black curves) and the exact solutions for τ_ν (top panel) and C_ν (middle panel). Vertical dashed lines mark the comoving frame velocity, v_c. The unphysical behavior of $\tau_{\nu,b} = 2\tau_{\nu,r}$ in the line wings is expected (see the discussion below equation (10)). Notice that the PPC model's doublet solution underestimates the true optical depth profiles measured from our simulations, while it overestimates the covering fraction profiles. In the second and third columns, C_ν is almost the same for the red and blue doublet transitions, whereas they significantly differ in the first panel where $\tau_\nu < 3$ at line center. Note that C_ν for the blue component is always close to its theoretical lower bound in the PPC model, $1 - I_r$ (dashed black curve). Along with the line profiles of each doublet component (blue and red), the bottom panel displays I_r^2 (magenta) to assess the importance of partial covering.

scenario for a BLR. Note, however, that TI is but one mechanism to produce a multiphase flow. Others that have been considered in the context of AGNs include clouds uplifted from the surface of an accretion disc by the ram pressure of a centrifugally driven MHD wind (e.g., Emmering et al. 1992; Kartje, Kónigl, & Elitzur 1999; Everett, Kónigl, & Kartje 2001), transient density enhancements produced by turbulence (e.g., Bottorff & Ferland 2001) in a radiatively driven wind, and a failed dusty wind (Czerny & Hryniewicz 2011; Czerny et al. 2015).

The absorption line profiles calculated herein can be expected to be representative of those produced by other multiphase flows, provided the clumpy gas is only moderately optically thick ($\tau_\nu \lesssim 5$) and subsonic with respect to its surroundings. Moreover, because these are local hydrodynamical simulations and the governing equations are Galilean invariant, our results apply equally well to clumps embedded in a highly supersonic outflow.

An important result from this work is that a complicated velocity field is not accompanied by a complicated line profile. Quite the contrary, the most chaotic flow regime produces the most symmetric line profiles: in the final two panels of the slab case with a variable flux (see Figure 3), the profile $I_r - I_b$ is single peaked and featureless. This is simply because the velocities of the clumps have been randomized and therefore (i.) any local acceleration signature has been lost and (ii.) the width of the absorption lines are set by thermal broadening alone because the local velocity field is subsonic. This result is consistent with several studies that have invoked 'microturbulence' to broaden line profiles, as the level of microturbulence required is supersonic (e.g., Horne 1995; Bottorff et al. 2000; Bottorff & Ferland 2002; Baldwin et al. 2004; Kraemer et al. 2007). Since it is unclear how supersonic motions can arise and persist (e.g., Kraemer et al. 2012), it is more likely that broad absorption lines are the result of ion opacity being spread over a wide range

of bulk velocities that are naturally present in a large scale outflow.

In addition to line profiles maintaining their smooth shapes before and after the onset of cloud disruption, it is important to point out that they mostly retain their strengths also, aside from a small amount of variability (recall §3.4). Evidently, the existence of a morphologically in tact cloud is not important; preservation of the mass fraction (or equivalently the filling factor) of warm gas is all that really matters, for then the overall ionization state will be unaffected. In part, this result is due to the fact that the hot gas in our simulations has a non-negligible optical depth, as revealed in §3.3, so that significant absorption still takes place in the absence of cloud material. Thus, the maintenance of line strengths may to some degree be a limitation of our simulations, as the hot gas is only about 5 times hotter than the warm gas and is therefore still cool enough to host O VIII ions. Nevertheless, the relatively high optical depth of the inter-cloud gas in these simulations may mimic the presence of a much larger column of very optically thin gas. Moreover, it is quite possible that cloud formation sites for warm absorbers indeed have low optical depth contrasts since resonance line opacities in the X-ray are typically much smaller than those in the optical or UV (e.g., Kallman 2010).

UV lines in BAL outflows, on the other hand, are more likely to be very optically thick if the absorption sites are produced by clouds (e.g., Arav & Li 1994). More work is required to produce synthetic line profiles for the common UV doublet lines. This requires two advances: (i.) much higher resolution simulations to resolve the high temperature and density contrasts. This will permit the modeling of a clumpy medium in which the hot gas is hot enough to be very optically thin and the warm gas cool enough to host UV lines. (ii.) solving the equations of radiation hydrodynamics using the variable Eddington tensor closure (e.g., Jiang et al. 2012; Proga et al. 2014), as optically thick clouds will cast shadows and this effect must be properly taken into account.

In this work we focused on a doublet line in the soft X-ray simply because O VIII Lyα was found to be the strongest line produced at these temperatures and photoionization parameters. Note that to resolve this doublet in actual spectra, a resolution of $R = \lambda/\Delta\lambda > 3500$ is required; this is beyond the capabilities of the X-ray Integral Field Unit being designed for the Athena+ mission (which has $R \lesssim 2400$ in the soft X-ray band; Barret et al. 2016), but it may be within the reach of Arcus (Smith et al. 2016) or Athena+'s high resolution X-ray grating spectrometer mission. Without resolving the doublet components, the only detectable cloud signature would be an asymmetric line profile: prior to complete cloud disruption, cloud acceleration will produce deeper absorption on the blue side of line center, as in Figure 2.

We can speculate that the common UV doublet lines may present even clearer evidence for cloud acceleration using the $I_r - I_b$ diagnostic. According to the PPC model, $I_r - I_b \approx C_\nu e^{-\tau_\nu}$ near line center, and since τ_ν can be very large, the dips in this profile should be very prominent. It is unclear, however, if outflows are sufficiently clumpy in the UV, as continuous disc wind models can explain broad absorption lines (e.g., Sim et al. 2010) and there is growing observational support for the line-driven disc wind scenario (e.g., Filiz Ak et al. 2014). Interestingly, there has been a recent attempt to measure the bulk acceleration of outflows using a large sample of C IV BAL troughs drawn from various Sloan Digital Sky Survey programs (Grier et al. 2016). We note that a local cloud acceleration signature is to be distinguished from such bulk acceleration signatures that arise on scales spanning the entire outflow. As we mention below, cloud acceleration can likely only be detected in narrow absorption lines.

5 CONCLUSIONS

Our simulations show that irrespective of the initial cloud geometry, cloud disruption generates vorticity and thus results in a complicated velocity field. Our main conclusion is that this process of mixing has little influence on the line profiles and ultimately makes them more symmetric. Were the warm gas to completely evaporate upon mixing, we would expect the line profile to significantly weaken, but it should still remain smooth since thermal broadening always dominates any bulk velocity broadening from a locally subsonic velocity field.

We confirmed our expectation that cloud acceleration imprints a deeper absorption signature on the blue side of line center before the cloud is completely disrupted. Our most interesting finding is that a sensitive spectral diagnostic for assessing the presence of cloud acceleration can be obtained by examining the difference $(I_r - I_b)$ of the absorption line profiles of a doublet line. This quantity appears in the 'doublet solution' of the commonly used PPC model (see equation (10)), and hence it should be possible to perform this analysis for common UV doublets.

The detection of a cloud acceleration signature can probably only come from narrow lines that are not much broader than a thermal width, as the signature would not be present for BALs, which likely originate from smooth outflows. Repeated detections are needed to infer the presence of cloud acceleration, as the location of the dip in $I_r - I_b$ should become increasingly blueshifted with time. Behavior that would serve as evidence for cloud disruption is if the dip reverses its blueward trend or gradually disappears after being monitored on a regular (perhaps daily) basis. The detection of such a time-scale and the absence or presence of repeated episodes showing this effect would strongly constrain models for the AGN environment.

Finally, we showed that in our simulations, line strengths are more affected by cloud disruption than by changes in ionization in response to a (20%) variation in the ionizing flux. Absorption line variability that is correlated with fluctuations in the continuum light curve has recently been interpreted as evidence that changes in the ionizing continuum drives this variability (e.g., Filiz Ak et al. 2013; Wang et al. 2015; Goad et al. 2016), while the absence of such correlations is instead attributed to the transverse motion of clouds across the line of sight (e.g., Muzahid et al. 2016; Wildy et al. 2016). Cloud formation and subsequent disruption is also uncorrelated with ΔF_X and can occur entirely along the line of sight without clumps leaving the field of view. Thus, it is an alternative to the two most commonly invoked explanations for absorption line variability.

ACKNOWLEDGMENTS

TW thanks Sergei Dyda and Jenny Greene for discussions related to this work, as well as Pat Hall for discussions and helpful comments on the manuscript. We acknowledge support provided by the Chandra award TM6-17007X issued by the Chandra X-ray Observatory center, which is operated by the Smithsonian Astrophysical Observatory for and on behalf of NASA under contract NAS8-39073.

References

Arav, N., & Li, Z.-Y. 1994, ApJ, 427, 700
Arav, N., Korista, K. T., & de Kool, M. 2002, ApJ, 566, 699
Baldwin, J. A., Ferland, G. J., Korista, K. T., Hamann, F., & LaCluyzé, A. 2004, ApJ, 615, 610
Barai, P., Proga, D., & Nagamine, K. 2012, MNRAS, 424, 728
Barlow, T. A., & Sargent, W. L. W. 1997, AJ, 113, 136
Barret, D., Trong, T. L., den Herder, J.-W., et al. 2016, arXiv:1608.08105
Bautista, M. A., & Kallman, T. R. 2001, ApJS, 134, 139
Begelman, M. C., & McKee, C. F. 1990, ApJ, 358, 375
Begelman, M. C., & Silk, J. 2016, MNRAS,
Blondin, J. M. 1994, ApJ, 435, 756
Bottorff, M., Ferland, G., Baldwin, J., & Korista, K. 2000, ApJ, 542, 644
Bottorff, M. C., & Ferland, G. J. 2001, Bulletin of the American Astronomical Society, 33, 99.05
Bottorff, M., & Ferland, G. 2002, ApJ, 568, 581
Castor, J. I., Abbott, D. C., & Klein, R. I. 1975, ApJ, 195, 157
Castor, J. I., & Lamers, H. J. G. L. M. 1979, ApJS, 39, 481
Crenshaw, D. M., Kraemer, S. B., & George, I. M. 2003, ARA&A, 41, 117
Czerny, B., & Hryniewicz, K. 2011, A&A, 525, L8
Czerny, B., Modzelewska, J., Petrogalli, F., et al. 2015, Advances in Space Research, 55, 1806
de Kool, M., Korista, K. T., & Arav, N. 2002, ApJ, 580, 54
Emmering, R. T., Blandford, R. D., & Shlosman, I. 1992, ApJ, 385, 460
Everett, J. E., Königl, A., & Kartje, J. F. 2001, Probing the Physics of Active Galactic Nuclei, 224, 441
Field, G. B. 1965, ApJ, 142, 531
Filiz Ak, N., Brandt, W. N., Hall, P. B., et al. 2013, ApJ, 777, 168
Filiz Ak, N., Brandt, W. N., Hall, P. B., et al. 2014, ApJ, 791, 88
Ganguly, R., Eracleous, M., Charlton, J. C., & Churchill, C. W. 1999, AJ, 117, 2594
Goad, M. R., Korista, K. T., De Rosa, G., et al. 2016, ApJ, 824, 11
Grevesse, N., Noels, A., & Sauval, A. J. 1996, Cosmic Abundances, 99, 117
Grier, C. J., Brandt, W. N., Hall, P. B., et al. 2016, ApJ, 824, 130
Hall, P. B., Hutsemékers, D., Anderson, S. F., et al. 2003, ApJ, 593, 189
Hamann, F., Barlow, T. A., Junkkarinen, V., & Burbidge, E. M. 1997, ApJ, 478, 80
Horne, K. 1995, A&A, 297, 273
Jiang, Y.-F., Stone, J. M., & Davis, S. W. 2012, ApJS, 199, 14
Kallman, T., & Bautista, M. 2001, ApJS, 133, 221
Kallman, T. R. 2010, Space Sci. Rev., 157, 177
Kartje, J. F., Königl, A., & Elitzur, M. 1999, ApJ, 513, 180
Kinch, B. E., Schnittman, J. D., Kallman, T. R., & Krolik, J. H. 2016, ApJ, 826, 52
Kraemer, S. B., Bottorff, M. C., & Crenshaw, D. M. 2007, ApJ, 668, 730
Kraemer, S. B., Crenshaw, D. M., Bottorff, M. C., Turner, T. J., & Miller, L. 2012, AGN Winds in Charleston, 460, 57
Krolik, J. H. 1977, Physics of Fluids, 20, 364
Krolik, J. H. 1979, ApJ, 228, 13
Krolik, J. H. 1988, ApJ, 325, 148
Krolik, J. H. 1999, Active galactic nuclei : from the central black hole to the galactic environment /Julian H. Krolik. Princeton, N. J. : Princeton University Press, c1999.,
Kurosawa, R., & Proga, D. 2008, ApJ, 674, 97-110
Mathews, W. G., & Blumenthal, G. R. 1977, ApJ, 214, 10
Mathews, W. G. 1986, ApJ, 305, 187
Mościbrodzka, M., & Proga, D. 2013, ApJ, 767, 156
Muzahid, S., Srianand, R., Charlton, J., & Eracleous, M. 2016, MNRAS, 457, 2665
Owocki, S. P., Castor, J. I., & Rybicki, G. B. 1988, ApJ, 335, 914
Proga, D., Ostriker, J. P., & Kurosawa, R. 2008, ApJ, 676, 101-112
Proga, D., Jiang, Y.-F., Davis, S. W., Stone, J. M., & Smith, D. 2014, ApJ, 780, 51
Proga, D., & Waters, T. 2015, ApJ, 804, 137 (Paper 1)
Ramirez-Velasquez, J. M., Klapp, J., Gabbasov, R., Cruz, F., & Sigalotti, L. D. G. 2016, arXiv:1607.07785
Salz, M., Banerjee, R., Mignone, A., et al. 2015, A&A, 576, A21
Sim, S. A., Proga, D., Miller, L., Long, K. S., & Turner, T. J. 2010, MNRAS, 408, 1396
Smith, R. K., Ackermann, M., Allured, R., et al. 2016, Proc. SPIE, to appear
Stevens, I. R., & Kallman, T. R. 1990, ApJ, 365, 321
Stone, J. M., Gardiner, T. A., Teuben, P., Hawley, J. F., & Simon, J. B. 2008, ApJS, 178, 137-177
Turner, T. J., & Miller, L. 2009, A&ARv, 17, 47
Wang, J.-M., Du, P., Baldwin, J. A., et al. 2012, ApJ, 746, 137
Waters, T., & Proga, D. 2016, MNRAS, 460, L79
Wang, T., Yang, C., Wang, H., & Ferland, G. 2015, ApJ, 814, 150
Wildy, C., Landt, H., Goad, M. R., Ward, M., & Collinson, J. S. 2016, MNRAS, 461, 2085

APPENDIX A: A MODIFIED DOUBLET SOLUTION

Here we modify the PPC model to account for the non-negligible optical depth in the hot gas, $\tau_{\nu,\min}$:

$$I_r = (1 - C_\nu)e^{-\tau_{\nu,\min}} + C_\nu\, e^{-\tau_{\nu,r}},$$
$$I_b = (1 - C_\nu)e^{-2\,\tau_{\nu,\min}} + C_\nu\, e^{-2\,\tau_{\nu,r}}. \tag{A1}$$

This model still entails that a given sight line passes through either hot gas or warm gas, but not both. Dropping the frequency dependence of $\tau_{\nu,\min}$ and treating it as a constant free parameter, the modified doublet solution becomes

$$\tau_{\nu,r} = -\ln I_r - \ln\left[\frac{I_r\, e^{-\tau_{\min}} - I_b}{I_r\, e^{-\tau_{\min}} - I_r^2}\right],$$
$$C_\nu = \frac{1}{1 + (I_b - I_r^2)/(e^{-\tau_{\min}} - I_r)^2}. \tag{A2}$$

The brown dashed lines in Figure A1 show how the doublet solution changes as $\tau_{\min}$ is increased from 0.01 (thin brown line) to 0.1 (thick brown line). For $\tau_{\min} = 0.1$, the discrepancy between the doublet solution and the profiles for τ_ν and C_ν calculated from our simulations is significantly reduced. The agreement is not expected to become excellent since $\tau_{\min}$ should be frequency dependent instead of constant.

The modified solutions are truncated at frequencies on either side of line center where $e^{-\tau_{\min}} = I_r$, since by equation (A2), C_ν vanishes at these points. Notice that C_ν for the modified solutions with $\tau_{\min} = 0.1$ can lie beneath $1 - I_r$;

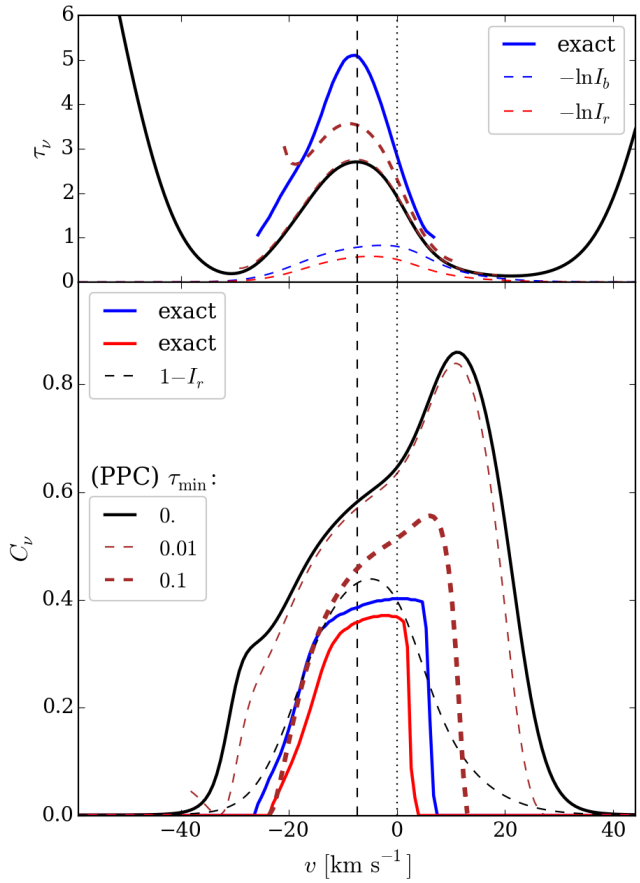

Figure A1. Same as the top two middle panels of Figure 6, but in addition showing two modified doublet solutions (dashed brown lines) that account for a nonzero value of $\tau_{\rm min}$. These modified solutions also show unphysical behavior in the line wings, but we have truncated these curves for clarity. This plot demonstrates that the discrepancy between the PPC model and the exact solutions becomes less with the modified doublet solution.

this lower bound holds only for the original doublet solution. Also, the correction term for the optical depth now demands $I_b \leq I_r\, e^{-\tau_{\rm min}}$, and this should be interpreted as placing an upper bound on $\tau_{\rm min}$, namely $\tau_{\rm min} \leq -\ln(I_b/I_r)$. Finally, by subtracting the expressions in equation (A1), an extra term appears that will be negligible for $\tau_{\rm min} \lesssim 0.1$, so as to retain self-consistency in our application of the PPC model to qualitatively understand the behavior of $I_r - I_b$.